

## Order and disorder in fully hydrated unoriented bilayers of gel phase dipalmitoylphosphatidylcholine

W.-J. Sun,<sup>1</sup> R. M. Suter,<sup>1</sup> M. A. Knewtson,<sup>1</sup> C. R. Worthington,<sup>2</sup>  
S. Tristram-Nagle,<sup>2</sup> R. Zhang,<sup>1</sup> and J. F. Nagle<sup>1,2</sup>

<sup>1</sup>*Department of Physics, Carnegie Mellon University, Pittsburgh, Pennsylvania 15213*

<sup>2</sup>*Department of Biological Sciences, Carnegie Mellon University, Pittsburgh, Pennsylvania 15213*

(Received 11 June 1993; revised manuscript received 13 January 1994)

We have performed x-ray scattering measurements of the wide-angle region of the gel phase of fully hydrated unoriented multilamellar vesicles of dipalmitoylphosphatidylcholine that quantitate two satellite peaks in addition to the usual (20) and (11) peaks. All the peaks in the wide-angle region are adequately fit using an electron density model consisting of straight chains with a terminal methyl gap and a head group term. The fit yields chains of length close to 20 Å that are tilted by  $\theta_t = 31.6^\circ$  toward nearest neighbors, at 24 °C. The fit also requires that the two monolayers in the bilayer are slightly offset rather than collinear. Subtraction of the fitted peak scattering and the background scattering obtained from samples with no lipid indicates that there is considerable broad diffuse scattering underlying the prominent peaks, thus providing a measure of the disorder in gel phase bilayers. The result that the head group term required to fit the wide-angle peaks is smaller than the corresponding head group term required to fit the low-angle reflections suggests that there is less order in the head groups than in the chains. However, the large amount of diffuse scattering appears to require disorder in both the chain and head regions.

PACS number(s): 87.22.Bt, 87.64.Bx, 78.70.Ck, 61.30.Eb

### I. INTRODUCTION

Fully hydrated lipid bilayers are of interest in biophysics because they are the structural basis of biomembranes. This has led to many structural and thermodynamic studies of model membrane systems [1–23]. These systems possess some order in the sense of having a layered structure and biophysical x-ray studies have focused upon this order. However, these fully hydrated systems are also disordered enough not to form crystals, and this disorder is undoubtedly important to biological function. The characterization of both the order and the disorder inherent in such partially ordered, anisotropic systems is clearly an appropriate topic for biological physics.

This paper studies the wide-angle scattering from the gel phase of dipalmitoylphosphatidylcholine (DPPC) lipid bilayers. This particular thermodynamic phase of this particular lipid has been perhaps the best characterized of all the lipid phases. There are two reasons for adding this study. The first is the occurrence of two small satellite peaks that have previously been ignored in structural analyses of unoriented samples. We show that refinements of the conventional model that treat the gel phase as an ordered two-dimensional crystal can account quantitatively for all the peaks. However, the conventional models cannot account for all the scattering. The peaks in the wide-angle region appear to be underlain by extensive broad scattering that is conventionally described as diffuse scattering caused by disorder. The second reason for this study is to emphasize this disorder in gel phase lipid bilayers and to begin to explore it.

The experimental system that is most reproducible and easiest to form in the laboratory is the fully hydrated

multilamellar vesicle that is basically an unoriented lyotropic smectic liquid crystal that scatters x rays in a powder pattern. Some kinds of structural information, such as the tilt angle  $\theta_t$  of the hydrocarbon chains, have been thought to be obtainable only from oriented samples, but these are somewhat more difficult to prepare and there is concern that the substrate may affect the properties of thin samples [16,17]. One of the purposes of this paper is to show that  $\theta_t$  can also be obtained from unoriented powder samples, and that this value of  $\theta_t$  agrees very well with our recent studies of oriented samples [16]. The value of  $\theta_t$ , along with low-angle lamellar diffraction and macroscopic volume measurements, is central to obtaining the ordered, average structure of gel phase lipid bilayers [18], and it is appropriate to obtain it for both oriented and unoriented bilayers. However, unoriented samples yield considerably more than a mere confirmation of the results from oriented samples. It may seem surprising that we can extract more information from powder averaged samples. The reason is that even the best oriented samples have some mosaic spread that degrades the data, whereas unoriented samples, while losing information about anisotropy, are less subject to such artifacts and they can be thicker allowing for better counting statistics with less radiation damage.

After presenting experimental details in Sec. II, Sec. III presents the wide-angle data. A simple strategy for dealing with these data from partially ordered systems is presented in Sec. IV followed by a detailed presentation of a model for the average order in Sec. V. The physical origin of the various peaks, especially the satellite peaks, is discussed in Sec. VI in terms of the simplest possible model. In Sec. VII the results of detailed fits to the data

are reported using the full model presented in Sec. V and the values of the parameters in the model are interpreted in terms of bilayer structure. An initial attempt is then made in Sec. VIII to understand the diffuse scattering, defined by subtracting the model and the background scattering from the data. A discussion that includes comparison with some other studies is given in Sec. IX.

## II. MATERIALS AND METHODS

### Phospholipid samples

DPPC (Lot #160 PC-176) was purchased from Avanti Polar Lipids (Birmingham, AL) and used without further purification. Samples were prepared for x-ray scattering by weighing water and lipid in a 3:1 (w:w) ratio. The lipid was hydrated by cycling it three times between 80 °C and 5 °C with 5 min of vortexing at each temperature. After hydration the sample was loaded into thin walled 1.0 mm glass x-ray capillaries (Charles Supper Co.). The capillaries had been precleaned by sequentially washing with chromic acid, acetone, and copious amounts of deionized water. After drying with nitrogen and flame sealing the capillaries at one end, they were filled with hydrated lipid using a 1.0 ml Hamilton syringe. Upon standing, these dispersions separate into a lipid rich phase and a clear water rich phase. In order to remove air bubbles, the capillaries were centrifuged for 10 min at 1100 g at room temperature. This amount of centrifugation did not overly compress the lipid, since upon additional standing for one week, the lipid settled further as indicated by the presence of a larger volume of water rich phase at the top of the capillary. X-ray scattering was obtained from the lipid rich phase and samples with either weight ratio gave the same low angle  $D$  spacing of 63.4 Å. In addition, the low angle  $D$  spacing was unaffected by centrifugation. After centrifugation the capillaries were flame sealed above the water layer, and this seal was dipped in Duco cement. After completion of the experiment, the continued presence of an excess water layer above the lipid was observed, confirming that the sample was fully hydrated during the course of the experiment. Then the lipid was removed from the capillary, dried under nitrogen and analyzed by thin layer chromatography using the solvent system chloroform:methanol:water (60:30:5). The chromatogram showed less than 0.2% lysolecithin formed during irradiation. Also, the positions and half widths of the first and second order low-angle peaks were identical before and after 48 h of irradiation, indicating that any degradation did not affect gel phase structure.

The lipid capillary was held upright in a custom built sample chamber made from aluminum with 1.5  $\mu\text{m}$  thick mylar windows (DuPont). A calibrated silicon diode (Type DT-470-CU-13) coated with Dow Corning heat sink compound was seated in a pocket in the aluminum block directly next to the capillary. The diode was connected to a Lake Shore Cryotronics Model DRC 84C Temperature Controller which monitored the temperature.

### X-ray scattering

Our principal measurements were carried out using a rotating anode x-ray source run at 35 kV and 150 mA and interfaced with a Huber four circle diffractometer via evacuated beampaths. Monochromatic copper  $K\alpha$  radiation was obtained by diffraction from a vertically bent graphite monochromator. Several different input and diffracted beam collimation and detection schemes were used, as described below. On the input side, two sets of  $xy$  slits, separated by 500 mm, define the beam size and divergence in the in-plane and out-of-plane directions. The four slit openings will be referred to as  $S_{mh}$ ,  $S_{mv}$ ,  $S_{sh}$ , and  $S_{sv}$ , where the  $m$  subscript refers to the slits nearest the monochromator,  $s$  to the slits nearest the sample,  $h$  is the horizontal (in-plane) opening, and  $v$  is the vertical (out-of-plane) opening. Slits after the sample eliminated extraneous scattering from air. An  $xy$ -slit set before the detector was also used to reduce extraneous radiation and to define the out-of-plane divergence.

For most measurements in the wide angle region, a Braun linear position sensitive detector (PSD) was placed on the detector arm of the diffractometer at a distance of 572 mm from the sample center. All vertical slit openings were 4 mm.  $S_{mh}$  and  $S_{sh}$  were set to 0.4 mm. Thus the beam size was less than the 1 mm capillary diameter and the in-plane divergence was 0.092° full width. Accounting for the finite beam size, the finite sample size and the divergence of the incoming beam leads to an estimate for the resolution half width at half maximum (HWHM) of 0.08° in  $2\theta$  which is expected to be an overestimate.

Some additional measurements used two other setups. First, to verify the background scattering obtained with the PSD, low resolution data (0.14° HWHM) were also taken for  $2\theta$  from 1° to 55° using a graphite crystal analyzer. To resolve fully the sharp (20) peak, the F-3 beamline at CHESS was used with silicon monochromator, silicon analyzer crystal and photomultiplier detector. This setup had a resolution of 0.004° HWHM at  $\lambda = 1.2148$  Å.

We carried out a limited set of measurements in the low-angle region to verify that samples were in the fully hydrated state and to check for effects of radiation damage. These measurements used the PSD with slits configured in the same way as for the wide-angle measurements. Some smearing of peaks on the low-angle side occurs in this configuration; we obtained best estimates for the  $D$  spacing by extrapolating the fitted peak positions to the higher order limit using model calculations of the smearing effect [16]. While this procedure yields only approximate values, it is reliable for comparing fresh samples with those which have been exposed to the x-ray beam for substantial periods. All data reported here are from samples for which no discernible shift in  $D$  spacing or broadening of the low- or wide-angle peaks could be detected after measurements were completed.

## III. DATA

Our best resolved data over a broad range, shown in Fig. 1, were obtained at  $T = 24$  °C with the rotating anode

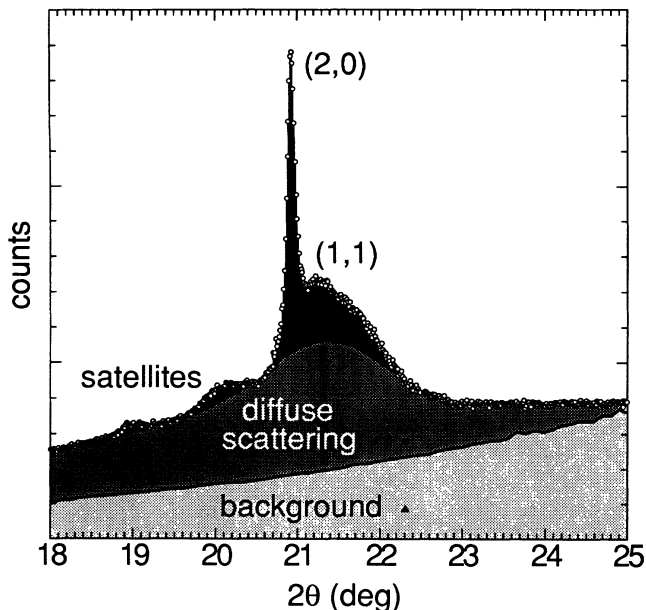


FIG. 1. Wide-angle scattering intensity versus scattering angle  $2\theta$  (open circles) taken with graphite monochromator and PSD 572 mm from the sample. Slits were configured to yield resolution  $0.068^\circ$  HWHM, which is the width of the unresolved (20) peak. The area in black is interpreted as the peak scattering. The temperature was  $24^\circ\text{C}$ . At  $2\theta = 22.3^\circ$  the solid square shows the scattering from a capillary filled with water and the solid triangle shows the scattering from a capillary in air.

ode source using the PSD. The sharp peak is usually identified as the (20) peak; the use of only two Miller indices indicates that this is scattering from along a Bragg rod due to a basically two-dimensional system rather than scattering from a Bragg peak due to three-dimensional order, as will be elaborated in Sec. V. The (20) peak was always centered very close to  $20.9^\circ$ , corresponding to  $d_{20} = 4.25 \text{ \AA}$ . In these data, the (20) peak has HWHM of  $0.06^\circ$ , which is close to our estimated instrumental resolution. Data that focussed on the (20) peak were also obtained at CHESS with resolution  $0.004^\circ$  HWHM. These data (not shown) yield an intrinsic linewidth of  $\Delta q$  that corresponds to  $0.015^\circ$  HWHM, indicating that order in the (20) direction within the membrane plane persists over length scales greater than  $2900 \text{ \AA} = 2\pi/\Delta q$ . A much broader peak occurs with a maximum near  $2\theta$  equal to  $21.3^\circ$ , although for one of our three samples this peak had moved to about  $21.5^\circ$ . This is usually identified as the (11) peak.

Figure 1 shows two smaller peaks in the  $2\theta$  range of  $20.5^\circ$ – $18.5^\circ$ . Below  $18.7^\circ$  the scattering is smooth and gradually decreasing (data only shown to  $18.0^\circ$ ). The two smaller peaks will be called “satellites” because they are due to additional scattering from the (11) Bragg rod. These satellites were first reported by Mitsui [9] and they can be discerned in other data [21] but they have usually been ignored in data from unoriented samples. Although the signal to noise is not high for such small features, we have consistently seen these two satellites at the same

angles for different data sets and different samples. It should also be noted that the two satellites appear to be sharper with more prominent maxima when observed on film or when the film is densitometered and the densitometer data are viewed on a computer screen. However, this sharpening is an optical illusion since numerical plots of the digitized densitometer data are very similar to the data shown in Fig. 1.

Background scattering arises from the glass capillary, air and the water. The background scattering curve shown in Fig. 1 was obtained from samples consisting of only water in the capillary and of only air in the capillary; data points at one angle are shown in Fig. 1. Since the ratio of water to lipid in the lipid samples was about 3 to 1, the true background was chosen to lie  $3/4$  of the way from the air+capillary data to the water+capillary data. Care was taken to normalize counting times and beam intensity for the control samples. The background scattering taken with the PSD and shown in Fig. 1 are in satisfactory agreement with background scattering obtained using a graphite analyzer crystal (data not shown). The difference between the total scattering and the background scattering becomes practically zero between  $25^\circ$  and  $30^\circ$ . It then increases between  $35^\circ$  and  $40^\circ$ , though it remains less than 20% as large as the difference near  $21^\circ$ . The difference between total scattering and the background scattering also continues to decrease for smaller  $2\theta$  than shown in Fig. 1.

#### IV. STRATEGY

The sharpness of the (20) peak suggests that there is order in these samples that extends over rather long distances;  $2900 \text{ \AA}$  is over 300 molecular nearest neighbor distances. This suggests that a reasonable starting point is to model the system as a crystal. As is already well known, however, the order that is reported by the wide-angle data in Fig. 1 is not three dimensional but consists of in-plane or two-dimensional order [7,14,3,22,12,16]. Thus, the starting point will be a two-dimensional crystal model. Strictly speaking, it is not possible to have true long range crystalline order in two dimensions [24]. However, if the decay distance of the short range order is large compared to the inverse instrumental resolution width, then the scattering will be close [25] to that from two-dimensional crystal models, which therefore remain the appropriate starting point.

The strategy we used was to start with the simplest basic two-dimensional crystal model (details of the 2D crystal models will be given in the next section) to see how well it could account for the data in Fig. 1. As is well known [7,14,3,8] this model predicts a sharp (20) peak and a broad (11) peak. As is not as well known, this model also predicts satellite peaks. This reinforces the hypothesis that the two-dimensional (2D) crystal model is an appropriate starting point. However, there were two major quantitative discrepancies. The first was that the exact positions of the satellite peaks were not in good agreement with the data. This is not surprising since the detailed nature of lipid bilayers suggests many refinements to the simplest 2D crystal model. As we will

show in Sec. VII, our refinements overcome this discrepancy completely. Specifically, we are able to obtain a model that gives that portion of the scattering indicated by the black areas in Fig. 1.

The second major discrepancy was that there is a large amount of scattering that is not accounted for, either by the simplest crystal model, or by any refinement of the 2D crystal model that we can imagine. This scattering is indicated by the dark gray area in Fig. 1. Because this scattering is very broad with no sharp peaks, we suggest that it be identified as diffuse scattering.

Formally, we are therefore dividing the total scattering  $I$  (after background subtraction) into peak scattering  $I_{\text{peak}}$  and  $I_{\text{diffuse}}$  where, as usual,

$$I(\mathbf{q}) = \int e^{i\mathbf{q}\cdot\mathbf{r}} \langle \rho(\mathbf{r}_1) \rho(\mathbf{r}_2) \rangle d\mathbf{r}_1 d\mathbf{r}_2, \quad (1)$$

where  $\mathbf{r} = \mathbf{r}_1 - \mathbf{r}_2$ . Writing

$$\langle \rho(\mathbf{r}_1) \rho(\mathbf{r}_2) \rangle = \langle \rho(\mathbf{r}_1) \rangle \langle \rho(\mathbf{r}_2) \rangle + [\langle \rho(\mathbf{r}_1) \rho(\mathbf{r}_2) \rangle - \langle \rho(\mathbf{r}_1) \rangle \langle \rho(\mathbf{r}_2) \rangle], \quad (2)$$

where the term in square brackets is the pair correlation function  $C(\mathbf{r}_1, \mathbf{r}_2)$  (which can also be written as  $\langle \delta(\mathbf{r}_1) \delta(\mathbf{r}_2) \rangle$ , where  $\delta(\mathbf{r}) = \rho(\mathbf{r}) - \langle \rho(\mathbf{r}) \rangle$ ), the total scattering  $I(\mathbf{q})$  can be written as a sum [26] of  $I_{\text{peaks}}$  and  $I_{\text{diffuse}}$ , where

$$I_{\text{peaks}} = \left| \int e^{i\mathbf{q}\cdot\mathbf{r}} \langle \rho(\mathbf{r}) \rangle d\mathbf{r} \right|^2 \quad (3)$$

depends only upon the average structure  $\langle \rho(\mathbf{r}) \rangle$ , which is assumed to be accurately described by a 2D crystal model, and

$$I_{\text{diffuse}} = \int d\mathbf{r}_1 \int d\mathbf{r}_2 e^{i\mathbf{q}\cdot\mathbf{r}} C(\mathbf{r}_1, \mathbf{r}_2), \quad (4)$$

which depends upon pair correlations which report fluctuational disorder in the bilayer.

The formalism in the preceding paragraph raises two issues. The first issue refers back to the first paragraph in this section: the possibility that no formal separation between peak scattering (i.e., Bragg rod scattering) and diffuse scattering can be performed because there are no 2D crystals due to long wavelength phonons. The consequences for scattering have been shown [25] to be power law tails added on to basically Gaussian peaks. These tails are important aspects of partially ordered low-dimensional physical systems. However, such tail scattering due to long wavelength phonons associated with the correlation length greater than 2900 Å would be expected to be highly concentrated near the Bragg rods and the total scattering in the tails would be expected to be small compared to the scattering under the central peaks. It would not appear that such tails would be able to account for the broad diffuse scattering indicated in Fig. 1. Instead, we suggest that most of the broad scattering is due to breakdown of order at much shorter distances. With molecules as complex as lipids, some portions may be packed in arrays fairly well ordered over large distances while other parts may be, at the same time, rather disordered. This disorder would

probably include many other fluctuations that are not directly coupled to the (20) peak order, such as head group orientations and rotations of the molecules and/or the hydrocarbon chains. This picture leads us back to the separation formalism embodied in the preceding paragraph.

If we now accept the separation formalism, then the second issue is a practical one. Where should one draw the curve between peak and diffuse scattering? Clearly, this curve is arbitrary unless one has a model that will give either the peak scattering or the diffuse scattering. Our approach indicated above is to obtain the best peak scattering from a 2D crystal model and to subtract it from the data to obtain the diffuse scattering. We turn first, in the next section, to a description of the 2D crystal model that we employed and then in Secs. VI and VII to the problem of obtaining the best values of the model parameters. Then, the subtraction of the peak scattering can be performed to obtain the diffuse scattering shown in Fig. 1.

## V. MODEL

The gel phase of lipid bilayers has been characterized for many years as having conformationally ordered, nearly *all-trans* hydrocarbon chains that pack into ordered arrays that give rise to the (20) and (11) peaks in Fig. 1 [7,14]. These ordered hydrocarbon chains may be tilted in various directions with respect to the nearly hexagonal lattice of packed chains [12]. However, it has been known for a long time that the fully hydrated gel phase of DPPC is characterized by the hydrocarbon chains being tilted towards nearest neighboring chains [7]. It has also been known that each bilayer scatters independently in the wide-angle region due to lack of registry of individual molecules across the aqueous spaces [7,14]. Since our data will fully confirm these two results, the exposition of the theory will assume them.

Figure 2 provides three views of the model of the gel phase lipid bilayer used in this paper. This model consists of chains and heads. The chains are straight, thin rods of electron density that are tilted by  $\theta_t$ . Straight (*all-trans*) hydrocarbon chains have methylenes ( $\text{CH}_2$ ) spaced a distance 1.27 Å apart along the chain axis [27]. However, the terminal methyl ( $\text{CH}_3$ ) occupies roughly twice as much volume as the methylenes [28,29] while having one additional electron, so each chain is modeled with a gap of  $\frac{7}{8}1.27$  Å at the center of the bilayer. The length of each rod will be given as  $L$ . There is no reason for precise collinearity of pairs of chains from the opposing monolayers, so offsets,  $\Delta x_c$  and  $\Delta y_c$ , will be allowed as shown in Fig. 2. Use of a body centered rectangular unit cell (often referred to as orthorhombic) with sides  $a$  and  $b$  then yields the following electron density function for the chains for values of  $|z|$  between  $L_1 = \frac{7}{8}1.27 \text{ Å} \cos \theta_t$  and  $L_2 = \frac{L}{\cos \theta_t}$ :

$$\rho_c(x, y, z) = \frac{8}{1.27 \text{ Å} \cos \theta_t} \rho_{cr}(x, y, z), \quad (5)$$

where

$$\rho_{cr}(x, y, z) = \begin{cases} \delta\left(x - \frac{\Delta x_c}{2}, y - \frac{\Delta y_c}{2} - z \tan \theta_t\right) \\ \quad + \delta\left(x - \frac{\Delta x_c}{2} - \frac{a}{2}, y - \frac{\Delta y_c}{2} - \frac{b}{2} - z \tan \theta_t\right) & \text{for } z > 0, \\ \delta\left(x + \frac{\Delta x_c}{2}, y + \frac{\Delta y_c}{2} - z \tan \theta_t\right) \\ \quad + \delta\left(x + \frac{\Delta x_c}{2} - \frac{a}{2}, y + \frac{\Delta y_c}{2} - \frac{b}{2} - z \tan \theta_t\right) & \text{for } z < 0. \end{cases}$$

The electron density  $\rho_H(x, y, z)$  for head groups is represented by Gaussians centered at  $\pm z_H$  with widths  $\sigma_H$  in the  $z$  direction. Other data [2] indicate that the head groups are oriented more parallel than perpendicular to the bilayer, so the portrayal of the head groups in Fig. 2 may be visually unsettling. However, our data do not allow determination of the orientation of the head groups, i.e., the widths of the head groups in the  $x$  and  $y$  direc-

tions. We can only determine the  $z$ -direction distribution of electron density, so only this is shown in Fig. 2, which therefore does not imply that the head groups are oriented perpendicular to the bilayer. Offsets,  $\Delta x_H$  and  $\Delta y_H$ , are also allowed for the head groups. Head groups are only placed on the half of the chains associated with the corners of the rectangular unit cell. Quantitatively, we take

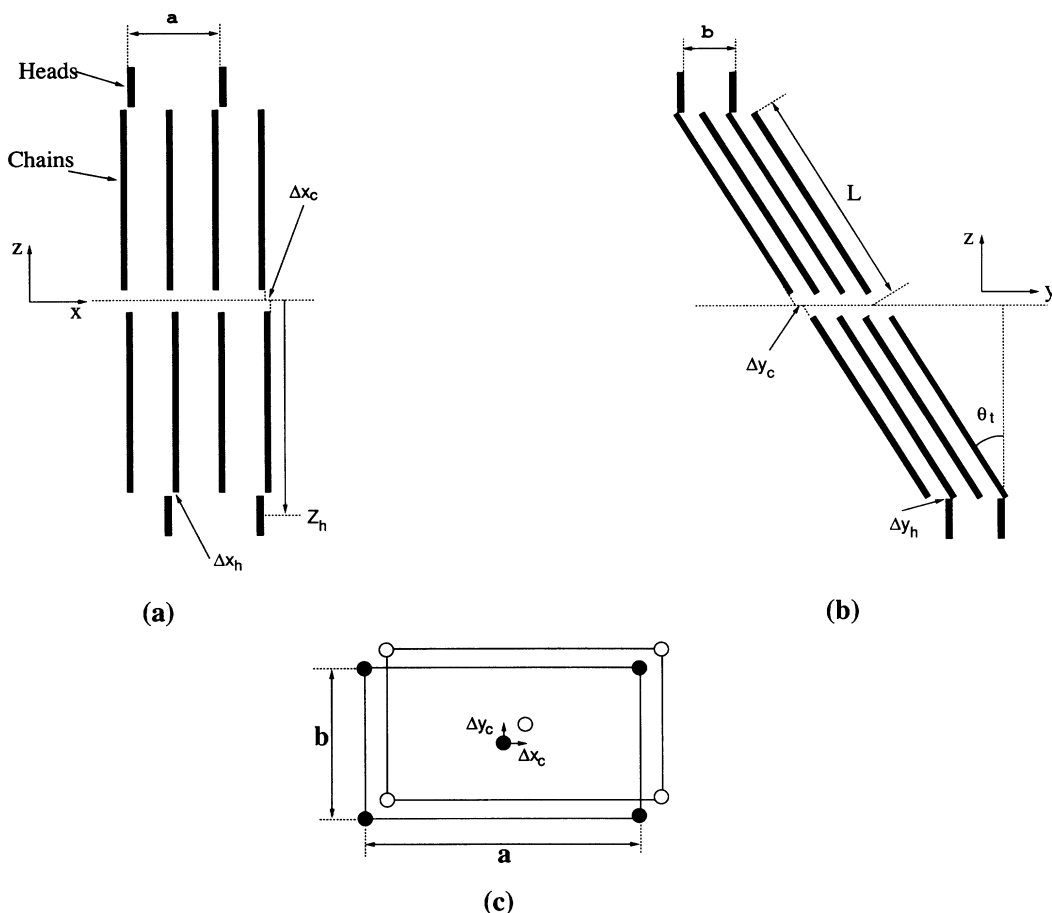


FIG. 2. Cross-sectional views of the model to fit the peak scattering. The drawing is to scale for the values of the parameters shown in Table I. (a) Projection onto the  $(x, z)$  plane. The chains are represented by long thin black rectangles and the head groups are represented by shorter gray rectangles.  $\Delta x_c$  is the chain offset,  $\Delta x_h$  is the head offset,  $Z_h$  is the peak position of the head group Gaussian and  $a$  is the unit cell dimension in the  $x$  direction. (b) Projection onto the  $(y, z)$  plane showing the tilt angle  $\theta_t$  and the length  $L$  of the chains.  $\Delta y_c$  is the chain offset,  $\Delta y_h$  is the head offset and  $b$  is the unit cell dimension in the  $y$  direction. (c) Projection onto the  $(x, y)$  midplane showing the body-centered two-dimensional unit cell. The filled (open) circles are the projections of the hydrocarbon chains from the upper (lower) monolayer, respectively, to show the offsets  $\Delta x_c$  and  $\Delta y_c$ . The scale for this projection is three times the scale for the preceding two projections. Only the  $z$  component of the head group electron density distribution is represented, so this figure does not imply that the head groups are perpendicular to the bilayer.

$$\rho_H(x, y, z) = \frac{n_H}{\sigma_H \sqrt{2\pi}} \left\{ \exp\left[\frac{-(z - z_H)^2}{2\sigma_H^2}\right] \times \delta\left(x - \frac{\Delta x_H}{2}\right) \delta\left(y - \frac{\Delta y_H}{2}\right) + \exp\left[\frac{-(z + z_H)^2}{2\sigma_H^2}\right] \times \delta\left(x + \frac{\Delta x_H}{2}\right) \delta\left(y + \frac{\Delta y_H}{2}\right) \right\}. \quad (6)$$

Periodicity with spacing  $a$  in the  $x$  direction and  $b$  in the  $y$  direction gives two Laue equations for x-ray scattering

$$aq_x = 2\pi N \text{ and } bq_y = 2\pi M, \quad (7)$$

which define the Bragg rods. If there are two equivalent substituents per unit cell that form a rectangular body centered lattice, as in Eq. (5), then  $N + M$  must be even and the two major wide-angle peaks are for  $(MN)$  equal to (20) and (11). This even constraint could be broken by inequivalent ordering of the chains as in polymethylene, but even there the (20) and (11) peaks are by far the strongest peaks [27]. The  $N + M$  even constraint could also be broken by ordered head groups as embodied in Eq. (6) and Fig. 2; we will return to this possibility later. For now let us note that this makes no difference to the calculation of the intensities along the (20) and (11) Bragg rods.

To obtain the x-ray scattering from the electron density, a final integration must be performed in the  $z$  direction. Apart from an inconsequential factor corresponding to the  $x$  and  $y$  integrations, this yields a form factor amplitude  $F(q_z)$  along the  $q_z$  direction for each Bragg rod,

$$F(q_z) = \int_0^\infty \rho_z(z) e^{i(\gamma z + \phi)} dz + \int_{-\infty}^0 \rho_z(z) e^{i(\gamma z - \phi)} dz, \quad (8)$$

where  $\gamma = q_z + q_y \tan \theta$  and  $\phi = \frac{q_x \Delta x + q_y \Delta y}{2}$ , with  $q_x$  and  $q_y$  given by Eq. (7). The integration in Eq. (8) is best performed separately for heads and chains, each with their separate offsets,  $\Delta x$  and  $\Delta y$ , with the result

$$F(q_z) = \frac{16}{1.27 \text{ \AA } \gamma \cos \theta_t} [\sin(\gamma L_2 + \phi_c) - \sin(\gamma L_1 + \phi_c)] + 2n_H \cos(\gamma z_H + \phi_H) e^{-(q_z \sigma_H)^2 / 2}, \quad (9)$$

where  $\phi_c = q_x \Delta x_c + q_y \Delta y_c$ , and  $\phi_H = q_x \Delta x_H + q_y (\Delta y_H - z_H \tan \theta_t)$ .

Our samples are unoriented dispersions so the  $\mathbf{q}$ -space diffraction pattern given by Eq. (9) was powder averaged and the usual Lorentz correction was applied. This was accomplished by multiplying the square of Eq. (9) by the factor  $\frac{1 + \cos^2(2\theta)}{q q_z}$ , where the components of  $q$  are  $q_z$  in Eq. (9) and  $q_x$  and  $q_y$  in Eq. (7). The final  $1/q_z$  factor, due to powder averaging the Bragg rods, theoretically produces square root singularities when the rod crosses the equator at  $q_z = 0$ , but observation of such singularities would require zero intrinsic widths of the Bragg rods as well as perfect instrumental resolution.

## VI. ORIGIN OF THE SATELLITE PEAKS

The essential scattering pattern for the model in the previous section can be most easily seen in the simple limit when head groups, offsets, and methyl gaps in the middle of the bilayer are ignored. Then the scattering is from a planar array of rods of finite length  $2L$  all tilted with angle  $\theta$  towards nearest neighbors. The  $q$ -space pattern for such an array is shown in Fig. 3. Along each Bragg rod the intensity variation is just the square of a sinc function as one sees from Eq. (9). The maximum intensity along the (20) Bragg rod occurs on the equator,  $q_z = 0$ . Because the rods are tilted, however, the maximum intensity along the (11) and (1, -1) rods are displaced from the equator and are given by the relation  $\gamma = 0$ , where  $\gamma$  is defined after Eq. (8).

The powder averaged (1,1) and (1, -1) central peaks are broad because the magnitude of the  $q$  vectors to various parts of these peaks along the Bragg rod are substantially different. In contrast, the powder averaged (20) peak is much narrower because the magnitudes of all the  $q$  vectors to various parts of that peak are nearly the same.

The ‘‘single slit diffraction pattern’’ along each rod shown in Fig. 3 also has secondary maxima, and some of these are the satellite peaks observed in Fig. 1. The secondary maxima along the (1,1) and (1, -1) Bragg rods that are closer to the equator than the central peaks are the satellites that occur at smaller angles than the (20) and (11) peaks in Fig. 1. The  $1/q_z$  factor that appears in the powder averaging enhances the apparent intensity of these peaks, which is another way of saying that the

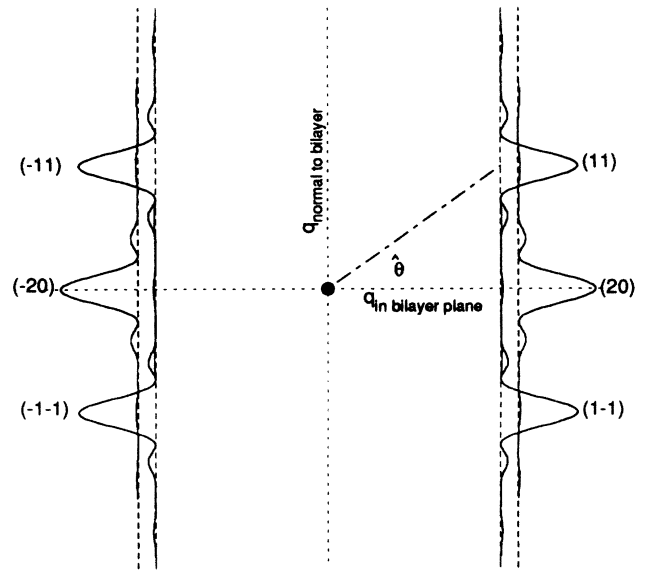


FIG. 3. The  $q$ -space pattern for the simplest model of chains tilted towards nearest neighbors. The locations of the Bragg rods are shown as vertical dashed lines. The intensities along these rods are shown as the horizontal distances between the solid curves and their underlying dashed lines. The angle  $\hat{\theta}$  appears in Eq. (10).

intensity is compressed into a smaller angular range because the difference in magnitudes of the  $q$  vectors for various parts of these secondary maxima is smaller the closer they are to the equator ( $q_z = 0$ ). Conversely, secondary maxima further from the equator will contribute broader and therefore lower peaks to powder scattering. With film data we observed one such satellite at higher angles than the (11) peak, but quantitative intensities could not be obtained. Similarly, satellites on the (20) Bragg rod are expected to be much less prominent than the central equatorial peak.

## VII. FITTING THE PEAKS

While the simple model described in the preceding section gives the overall qualitative features seen in Fig. 1, it does not give very good quantitative agreement with the scattering angles for the satellite peaks. In this section we demonstrate that the physically plausible refinements of the model described in Sec. V can yield quantitative agreement with all peak scattering.

Fitting the peaks in Fig. 1 with a model poses a problem because there are a number of parameters in any realistic model whose practical determination requires non-linear least squares fitting, but such fitting cannot be performed on the total measured scattering. We therefore used calculations for our model to establish criteria that allow reasonable guesses for the diffuse scattering curve. One key criterion was that peak scattering should fall to low values (though not necessarily exactly zero, *vide infra*) between the satellite peaks and between the first satellite and the (20) peak. Also, peak scattering should be small for  $2\theta$  larger than the (11) peak. Another key criterion is that the integrated intensity in the (11) peak should be about twice as large as the integrated intensity of the (20) peak. This ratio,  $R_{II}$ , should be exactly 2 if the electron density of the hydrocarbon chains is modeled as a  $\delta$  function rod as in Sec. V. We also performed calculations modeling the tails more accurately as stereochemically accurate zigzag chains. Then,  $R_{II}$  could vary by as much as 40%, but this much deviation of  $R_{II}$  from 2 requires full rotational order of the chains about their long axis in specific directions. There is evidence for some rotational order in the gel phase [30], but the rotational order is closer to fully disordered than to ordered, so the deviation of  $R_{II}$  from 2 is probably much smaller than 40%. For  $R_{II}$  to be close to 2, the diffuse scattering curve must have a broad peak under the (11) peak such as the one drawn in Fig. 1. Subtraction of this diffuse scattering curve from the measured scattering yields the peak scattering curve shown in Fig. 4.

In addition to the parameters defined in the model in the previous section, a parameter  $\sigma_{inst}$  for the instrumental resolution and a parameter  $\sigma_{11}$  for the intrinsic width of the (11) Bragg rod were allowed. Since the intrinsic (20) peak width is much narrower than the instrumental resolution, it was assumed to be zero.

Fits to the peak scattering in Fig. 4 were driven by the IMSL nonlinear least squares computer library routine UNLSF. The reduced  $\chi^2$  of the fit shown in Fig. 4

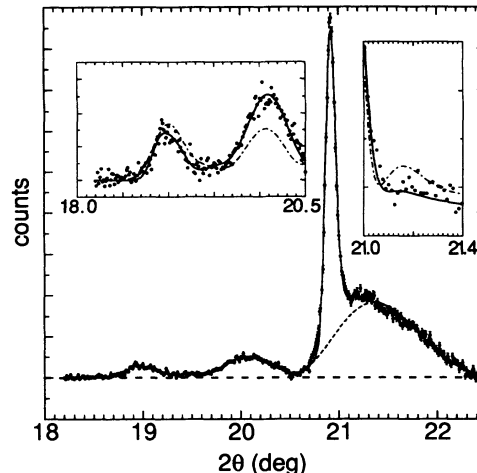


FIG. 4. Peak scattering, solid circles with error bars, from Fig. 1 and model fits from Sec. IV. Longer counting times in the satellite region account for the smaller error bars there. The solid line running within the error bars of most of the data points shows our best fit ( $\chi^2=2.03$ ). The dashed line shows the separate contribution from the (11) Bragg rod. The left hand inset expands the vertical scale for the satellite region with scattering angles between  $18^\circ$  and  $20.5^\circ$ . The right hand inset expands the region between  $21.0^\circ$  and  $21.4^\circ$ . The dot-dash lines in the insets show the suboptimal fit when the offsets were set to zero ( $\chi^2=5.79$ ).

was 2.03, which was quite good considering the intrinsic uncertainty in subtraction of the diffuse scattering. The largest systematic error in the fit is for  $2\theta$  between  $20.7^\circ$  and  $20.8^\circ$  on the low-angle side of the (20) peak. This could be due to omission from the fitting of the power law tails mentioned in Sec. IV. The values of the basic parameters determined by the fit shown in Fig. 4 are given in Table I. Two kinds of errors are shown in this table. The first set of errors was determined for one particular diffuse scattering curve in the usual way, namely, fits were performed in which one parameter was held fixed and all other parameters were then optimized. Those values of the fixed parameter that gave increases of 1 in  $\chi^2$  yield the first errors shown in Table I. The second set of errors was estimated by choosing two different diffuse

TABLE I. Results for fitted parameters to wide angle.

| Parameter       | Value                                      |
|-----------------|--|
| $d_{20}$        | $4.2440 \pm 0.0001 \pm 0.0004 \text{ \AA}$ |
| $d_{11}$        | $4.182 \pm 0.003 \pm 0.006 \text{ \AA}$    |
| $\theta_t$      | $31.6 \pm 0.1 \pm 0.2^\circ$               |
| $L$             | $21.32 \pm 0.07 \pm 0.5 \text{ \AA}$       |
| $\sigma_{inst}$ | $0.0578 \pm 0.0005 \pm 0.0014^\circ$       |
| $\sigma_{11}$   | $0.09 \pm 0.01 \pm 0.04^\circ$             |
| $\Delta x_c$    | $0.47 \pm 0.03 \pm 0.05 \text{ \AA}$       |
| $\Delta y_c$    | $0.64 \pm 0.07 \pm 0.13 \text{ \AA}$       |
| $n_H$           | $45 \pm 1 \pm 11$ electrons                |
| $z_H$           | $20.38 \pm 0.07 \pm 0.25 \text{ \AA}$      |
| $\sigma_H$      | $1.9 \pm 0.2 \pm 0.1 \text{ \AA}$          |
| $\Delta x_H$    | $0.73 \pm 0.06 \pm 1.0 \text{ \AA}$        |
| $\Delta y_H$    | $0.4 \pm 0.1 \pm 0.3 \text{ \AA}$          |
| $R_{II}$        | $2.01 \pm 0.08 \pm 0.12$                   |

scattering curves and comparing the values of the best fit parameters.

While the fit to the data is a complex interaction of all the parameters, there are some particular regions of the data that most strongly influence certain parameters. The values of  $d_{20}$  and  $\sigma_{\text{inst}}$  are quite well determined by the sharp (20) peak. The breadth of the central (11) peak is largely determined by twice the length  $L$  of the chains, which establishes the width of the central peak along the Bragg rod, and by the tilt angle  $\theta$  which determines how far this peak is displaced from the equator (*vide infra*). The correct value of  $L$  for all-trans hydrocarbon chains consisting of 14  $\text{CH}_2$  groups and a terminal  $\text{CH}_3$  is  $16(1.27 \text{ \AA}) = 20.3 \text{ \AA}$ . That the fitted value of  $L$  is slightly larger is quite satisfactory; it is consistent with the model chain including some of the carbonyl group.

A subtle but important relation concerns the "edge" angle  $2\theta_e$  corresponding to the  $q$  value where the (11) Bragg rod crosses the equator. For  $\theta < \theta_e$  there is no peak scattering except for resolution broadening of the square root singularity at  $\theta_e$ . The fact that our data are very smooth from  $18.8^\circ$  down to  $15.5^\circ$  (not all data shown in Fig. 1) suggests that  $2\theta_e$  is close to  $18.9^\circ$ . Identifying  $\theta_e$  provides the equatorial component  $q_{r,11} = \frac{4\pi}{\lambda} \sin \theta_e$  of the (11) peak. This allows one to determine  $\theta_t$  from the well-known relation [7,12,22]

$$\sin \hat{\theta} = \sqrt{1 - \left( \frac{q_{20}}{2q_{11}} \right)^2} \sin \theta_t, \quad (10)$$

where  $\hat{\theta}$  is the angle of the (11) peak in  $\mathbf{q}$  space defined by  $\cos \hat{\theta} = \frac{q_{r,11}}{q_{11}}$ . Although there is some uncertainty in estimating  $q_{11}$  because of the foot on the (20) peak between  $21.1^\circ - 21.3^\circ$ , even rough estimates without detailed fitting yield values of  $\theta_t$  of  $31^\circ - 32^\circ$ . This agrees very well with our recent work [16] on fully hydrated oriented DPPC bilayers which obtained the tilt angle  $\theta_t$  to be  $32.0^\circ \pm 0.5^\circ$  at  $19^\circ\text{C}$ . Even the slightly smaller values obtained in this fit to data at  $24^\circ\text{C}$  can be attributed to our earlier observation that the tilt angle decreases with increasing temperature [16]. Our earlier work also verified directly that the tilt is towards nearest neighbors. With such good agreement with known quantities, we believe that some of the values for additional parameters obtained for the first time are worthy of consideration.

The intrinsic linewidth  $\sigma_{11}$  of the (11) Bragg rod is another parameter that can be directly estimated by the breadth of the edge at  $2\theta_e$  of the second satellite. At first, we were concerned that the (11) Bragg rod requires a considerably larger intrinsic width than the (20) Bragg rod, but the data in Fig. 2(c) in Ref. [12] show the same comparison for oriented samples. An explanation for this is that there is likely to be a distribution of tilt angles  $\theta_t$ . Since the tilt angle probably depends upon competing interactions [16] that are small relative to the strong cohesive interactions that establish the wide-angle  $d_{11}$  and  $d_{20}$  spacings, the distribution of these latter spacings may be taken to be very narrow and can be ignored compared to the distribution of  $\theta_t$ . Therefore, the distribution of  $\theta_t$  gives rise to a distribution of (11) Bragg rods that cut

the equator at different angles  $\theta_e$  and this distribution in  $\theta_e$  determines  $\sigma_{11}$ . Using the relations in the preceding paragraph yields mean fluctuations in  $\theta_t$  of  $\pm 1.3^\circ$  about its average value given in Table I. Notice that the size of these fluctuations is distinct from the estimated error in the average value of  $\theta_t$ .

The insets in Fig. 4 show two regions where the fit is adversely affected by not allowing any offsets. This suggests that offsets not only could exist, but do exist. We originally drew the diffuse scattering curve in Figs. 1 and 4 so that the peak scattering would go to zero near  $19.5^\circ$  and near  $20.5^\circ$ , but this is not a necessity as seen from the fitted curves in Fig. 4. The reason for this is interesting and reveals some features that help to appreciate the effect of the offsets shown in Fig. 2. Figure 5 shows the form factors for the (1,1) and (1,-1) rods. Offsets lower the symmetry which only demands that the (1,1) and (-1,-1) rods have the same form factors and also that the (1,-1) and (-1,1) rods have the same form factors. To obtain the intensity, the individual form factors are first squared and then added because the scattering from the two rods comes from different regions in real space that scatter incoherently. Even though the intensity from each Bragg rod has zeros, the zeros occur for different values of  $q$  for the (1,1) and (1,-1) rods, so there are no zeros in the sum. Another reason that there are no zeros between the satellites in Fig. 4 is that both  $\pm|q_z|$  values contribute to the same powder averaged value of  $q$ . Another feature of interest in Fig. 5 is that the form factor is not symmetric along  $q_z$  as it would be for a sinc function which describes a simple array of rods with no offsets or head groups. The simple sinc functions have a maximum at the  $q_z$  indicated by the vertical dashed line near  $0.7 \text{ \AA}^{-1}$  in Fig. 5; this is the value of  $q_z$  that gives  $q = \frac{2\pi}{d_{11}}$ . With nonzero offsets the maxima in the form factors are displaced as shown in Fig. 5 and reflection symmetry about this  $q_z$  value disappears.

The electron densities perpendicular to the bilayer determined from the fit in Fig. 4 and Table I are shown in Fig. 6. The chain electron density has been normalized so that it gives the total number of electrons 248,

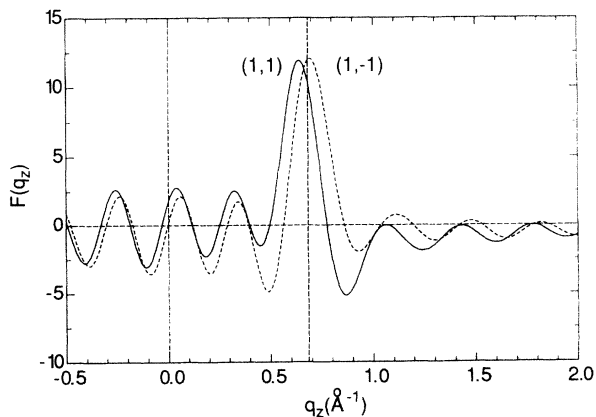


FIG. 5. The form factors  $F(q_z)$  along the (1,1) and (1,-1) Bragg rods for the parameters in Table I. One vertical dashed line at  $q_z = 0$  marks the equator and the other vertical dashed line at  $q_z = 0.684$  marks the value where  $q = 2\pi/d_{11}$ .

as in the chains (not including the first carbonyl carbon) when multiplied by the area per molecule  $A$  and then integrated along  $z$ . With this same normalization the number of electrons under the fitted head group peak is  $n_H^{\text{fit}} = 45.0$ . This may be compared to the number of electrons  $n_{\text{PO}_4} = 47$  in the phosphate,  $n_{\text{choline}} = 50$  in the choline and  $n_{\text{back}} = 67$  in the backbone which includes the first carbonyl carbons on the acyl chains, for a total number of electrons in the head  $n_H = 164$ . (Subtraction of that fraction of the carbonyl electrons that are included in the slightly larger  $L$  would only reduce this by 12.) That this actual  $n_H$  is considerably larger than the  $n_H^{\text{fit}}$  derived from the size of the fitted head group peak suggests that the head groups are more disordered than the tails so that they preferentially scatter diffusely rather than with coherent peak scattering.

Figure 6 also shows the electron density determined from our low-angle data [18]. The small mismatch with the wide-angle data in the chain region is due to use of a less accurate and smaller measurement of  $d_{11}$  in the earlier paper. The head group Gaussian from the low-angle data is larger by a factor of 1.24, containing about 56 electrons, than the head group Gaussian from the wide-angle fit in Fig. 4 that contains 45.0 electrons. Furthermore, 56 electrons is an underestimate of the number of electrons in the head group obtained from the low-angle fit because that Gaussian sits on a smooth “bridging” electron density that comes from a variety of molecular substituents such as water, chains, and head group contributions that are not included in the head group Gaussian. These latter head group contributions account for water and chains that have been displaced from the head group region and therefore the apparent head group Gaussian just accounts for electron density of the head groups in excess of the water and hydrocarbon chains.

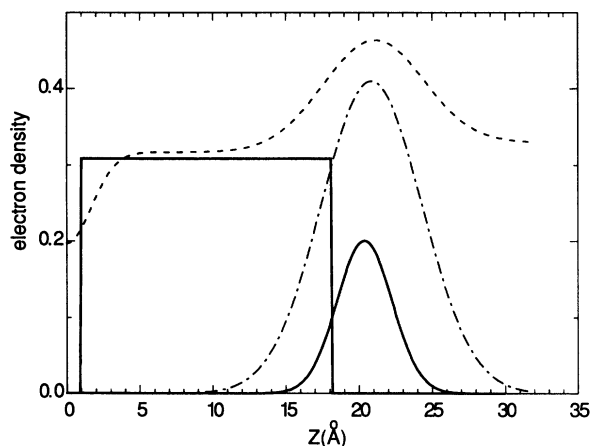


FIG. 6. Electron density  $\rho_z$ , in units of electrons/ $\text{\AA}^3$ , along the bilayer normal for half a symmetric bilayer, with the mid-plane (terminal methyl trough) at  $z = 0$ . The constant solid line shows the chain density and the solid Gaussian shows the head group contribution for the parameters in Table I. The electron density determined by our previous low-angle study (Ref. [18]) is plotted with a dashed curve and the low-angle head group contribution is plotted separately (dot-dash curve) for comparison with the wide-angle head group Gaussian.

To account for the total number of head group electrons, the low-angle Gaussian should be scaled by a factor of 2.9 for comparison with the wide-angle head group Gaussian. This is shown as the dot-dash Gaussian in Fig. 6. [The difference between the low-angle electron density (dashed line in Fig. 6) and the dot-dash Gaussian is the sum of the electron density of the chains and the water; this sum is positive as it must be.] Since the dot-dash Gaussian is much larger than the solid Gaussian obtained from the wide-angle fit, it can be concluded that, when normalized by the chain scattering, the head group electrons yield less peak scattering in the wide-angle region than in the low-angle region.

The quantities in Table I determined directly by the fit to the wide-angle data allow the determination of other interesting quantities for bilayer structure shown in Table II. The following elementary equations give the unit cell dimensions,  $a$  and  $b$ , and the area  $A_c$  perpendicular to the chain and the area  $A$  of the head group:

$$a = 2d_{20}, \quad b = \frac{d_{11}}{\cos \theta_t \sqrt{1 - \left(\frac{d_{11}}{2d_{20}}\right)^2}},$$

$$A_c = \frac{d_{20}d_{11}}{\sqrt{1 - \left(\frac{d_{11}}{2d_{20}}\right)^2}} \quad \text{and} \quad A = \frac{2A_c}{\cos \theta_t}. \quad (11)$$

Since the length of a methylene group is 1.27  $\text{\AA}$  along all-trans chains, the volume per methylene  $V_{\text{CH}_2}$  equals  $A_c \times 1.27 \text{\AA}$ . Using our current measurement of  $A_c$ , the ratio of methyl volume to methylene volume is determined from our previous low-angle diffraction work (see Fig. 2 in Ref. [18]) to be in the range 2.0–2.1, which also agrees with [28,29], and this yields  $V_{\text{CH}_3}$ . The hydrocarbon volume  $V_C$  consists of two chains, each with 14 methylenes and one methyl. The average thickness of the hydrocarbon region  $D_C$  is obtained from  $V_C/A$ . The volume of the head group  $V_H$  equals the measured volume [11] of the entire lipid  $V_L$  minus the volume of the chains  $V_C$ . The volume  $V_X$  of the unit cell comes from  $AD/2$  where our recent measurement of the low-angle  $D$  spacing [16] is given. Finally, the number of waters per lipid is given by  $(V_X - V_L)/V_W$  where  $V_W$  is

TABLE II. Other results.

| Parameter         | Value                          |
|-------------------|--------------------------------|
| $a$               | $8.4880 \pm 0.0008 \text{\AA}$ |
| $b$               | $5.64 \pm 0.02 \text{\AA}$     |
| $A_c$             | $20.40 \pm 0.04 \text{\AA}^2$  |
| $A$               | $47.9 \pm 0.2 \text{\AA}^2$    |
| $V_{\text{CH}_2}$ | $25.91 \pm 0.05 \text{\AA}^3$  |
| $V_{\text{CH}_3}$ | $53.1 \pm 1.3 \text{\AA}^3$    |
| $V_C$             | $829 \pm 4 \text{\AA}^3$       |
| $D_C$             | $17.3 \pm 0.2 \text{\AA}$      |
| $V_L$             | $1148 \pm 2 \text{\AA}^3$      |
| $V_H$             | $319 \pm 6 \text{\AA}^3$       |
| $V_X$             | $1518 \pm 9 \text{\AA}^3$      |
| $D$               | $63.4 \pm 0.1 \text{\AA}$      |
| $n_w$             | $12.6 \pm 0.4$                 |

the volume of a water molecule which is  $30.0 \text{ \AA}^3$  for this temperature of  $24^\circ\text{C}$ . Our previous estimates for many of the quantities in Table II [18] used wide-angle data that were not fully resolved from which we estimated a value of  $d_{11} = 4.12 \pm 0.02 \text{ \AA}$ , which is significantly smaller than the value of  $d_{11}$  from Table I. This difference is the primary reason that our previous [18] and current error bars do not overlap for the quantities  $A_c$ ,  $V_{\text{CH}_2}$ ,  $V_{\text{CH}_3}$ ,  $V_C$ , and  $V_H$ . There may, however, be variations from one sample to another that account for these differences in these latter quantities. We obtained a different data set at  $19^\circ\text{C}$  that gave results consistent with the values for most of the quantities in Table I, but which had  $d_{11} = 4.14 \text{ \AA}$ . This propagated values of  $A_c$ ,  $V_{\text{CH}_2}$ ,  $V_{\text{CH}_3}$ ,  $V_C$ , and  $V_H$  that are about midway between our previous results [18] and the results in Table II. Therefore, it might be appropriate to assign a wider range of uncertainty to these quantities.

### VIII. DIFFUSE SCATTERING

Our success in fitting the peak scattering in Fig. 1 suggests that our program of separating the total scattering into peak scattering and diffuse scattering is reasonable. It also suggests that the actual quantitative diffuse scattering curve is now reasonably reliable and can be used as a starting point for the discussion of diffuse scattering. Indeed, precision in the determination of the diffuse scattering curve will probably be much less important in discussing the diffuse scattering than it was in fitting the peak scattering. At this time the most remarkable aspect of the diffuse scattering is the large amount of it, as shown in Fig. 1.

At this point it may be useful to compare to the data in Fig. 2 of Ref. [12] which shows one nicely resolved satellite peak for oriented lipid samples. Although the lipid and the degree of hydration were different, it is still perhaps meaningful that there is a clear minimum between the central peak and the satellite peak on each Bragg rod in the scattering from the oriented samples. For the same magnitude of the scattering angle in Fig. 1 ( $2\theta = 20.4^\circ$ ) there is, in contrast, only a plateau in the scattering. Of course, the scattering in Fig. 1 comes from all  $q$  vectors with the same magnitude, so there is no necessity that there should be a minimum in powder samples even if there is a minimum along the Bragg rods. The two sets of data together suggest that a major part of the diffuse scattering comes from other parts of  $q$  space than along the Bragg rods. Since the Bragg rods are dominated by the chain packing and since the results in the preceding section suggest that the head group region is relatively more disordered at the  $4\text{-}5 \text{ \AA}$  length scale, it is reasonable that head groups may be a plausible starting point for this other diffuse scattering.

Let us therefore initiate a first exploratory search for the origin of the diffuse scattering by focusing upon the head group region. One reason for greater disorder in the head group region is simply the molecular nature of the lipid molecule, with one head for every two chains, so that, even if the chains were perfectly packed in an

hexagonal array, the heads could be represented as a disordered array of dimers connecting pairs of chains, as indicated in the inset to Fig. 7. Furthermore, the most electron dense part of the head group is the phosphate group. The position of this group, when projected onto the bilayer plane, is closer to the *sn*-1 chain than to the *sn*-2 chain. This suggests a simple model as a first approximation for head group diffuse scattering. Each head group represented by a dimer in the inset to Fig. 7 will have a differential scattering center located at only one end on the projection of the hexagonal array of chains. The array of dimers will be considered to be random with respect to orientation of the dimers and with respect to the electron dense ends.

For any model the total scattering is given by Eq. (1). For the simple model considered here,  $\mathbf{r}_1$  may be taken to be the origin and the double integral becomes a single sum over the triangular lattice,

$$I(\mathbf{q}) = \sum_n e^{i\mathbf{q}\cdot\mathbf{r}} \langle \rho(0)\rho(\mathbf{r}_n) \rangle. \quad (12)$$

The correlation function at the origin,  $\langle \rho(r_0)\rho(r_0) \rangle$  equals  $1/2$  because this is the probability that the electron dense phosphate end of the head group is at the origin. For nearest neighbor lattice sites on the triangular lattice the correlation function is  $\langle \rho(r_0)\rho(r_{nn}) \rangle$ , which can be calculated as a factor of  $1/2$  for the dense end at the origin and a factor of  $5/12$  for having a dense end at the nearest neighbor site. The reason that this latter probability is less than  $1/2$  is due to the fact that, if there is a dense end at the origin, then one of the nearest neighbor sites must have a nondense end while the other five neighbors have probability  $1/2$  of having a dense end. Fur-

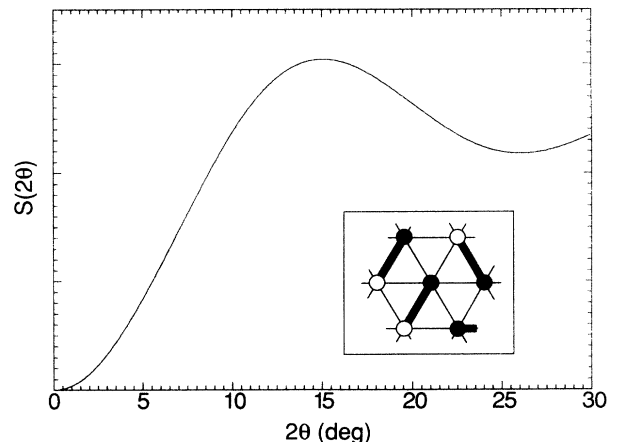


FIG. 7. Diffuse scattering  $S(2\theta)$  versus scattering angle  $2\theta$  predicted by a simple model for phosphate head groups indicated by the inset which represents an  $x$ - $y$  plane [see Fig. 2(c)] at the  $z$  level of the head groups. Each hydrocarbon chain projects to one of the lattice sites in the inset. Each phosphate group is represented by a solid circle near one chain and the position of the other chain in the same molecule is represented by an open circle connected to the phosphate group by a broad gray line.

ther neighbor correlations  $\langle \rho(r_0)\rho(r_{fn}) \rangle$  all have values of  $(1/2)(1/2)=(1/4)$ .

The sum in Eq. (12) may now be separated into two pieces. The first piece is a sum over all lattice sites  $n$ ,

$$I_P = \frac{1}{4} \sum_n e^{i\mathbf{q}\cdot\mathbf{r}}, \quad (13)$$

which yields a Bragg rod that has already been included in the peak analysis in the preceding section. The remaining terms can be written as a sum over nearest neighbors  $nn$ ,

$$I_D = \frac{1}{24} \sum_{nn} [1 - e^{i\mathbf{q}\cdot\mathbf{r}}], \quad (14)$$

and yield diffuse scattering.

In order to compare to Fig. 1 the diffuse scattering in Eq. (14) must be powder averaged. Ignoring atomic or molecular form factors, this yields

$$I_D = \frac{1 - \text{sinc}(bq)}{2}, \quad (15)$$

where  $b$  is the nearest neighbor distance which is also the unit cell dimension  $b$  used in the preceding section. Figure 7 shows  $S(q)$  from Eq. (15). Unfortunately, this result is not in good agreement with the diffuse scattering inferred from Fig. 1, suggesting that this simple model of positional disorder in the phosphate group is not the only cause of diffuse scattering.

An indication that the diffuse scattering is not likely to be due entirely to the head group region comes from the estimate that the wide-angle scattering under the peaks is only about 30-40% as large as the scattering labeled diffuse in Fig. 1, so the integrated peak scattering is only about 25% of the total scattering. As a rough approximation, let us suppose that this fraction  $f_P = 0.25$  of the scattering under the peaks can be represented as a superposition of the scattering from the heads and chains, as follows:

$$f_P = \frac{f_c n_c + f_H n_H}{n_P}, \quad (16)$$

where  $n_P = 412$  is the number of electrons in DPPC,  $n_c = 248$  is the number of electrons in the chains, and  $n_H = 164$  is the number of electrons in the heads. In this approximation the fractions  $f_c$  and  $f_H$  give estimates of the degree of order in the chain and head regions, respectively. From the fitting in the preceding section we have  $f_H n_H = 45 f_c$ , so  $f_c = 103/(248 + 45) = 0.35$  and  $f_H = 0.10$ . This rough estimate yields larger values of  $f_c$  than  $f_H$ , in agreement that the head groups are more disordered than the chains. The small value of  $f_c$  also suggests that even the chains are relatively disordered and this disorder must be included in order to account for the diffuse scattering. The appearance of a diffuse scattering peak centered near the (20) and (11) peaks is also an indication of chain disorder.

## IX. DISCUSSION

The gel phase has usually been thought of as a fairly well-ordered phase because the hydrocarbon chains are nearly *all-trans*, in contrast to the fluid  $L_\alpha$  phase which is rotamerically, i.e., conformationally, disordered [10]. This difference in rotameric ordering is clearly proven by the appearance of sharp peaks in the wide-angle region of the gel phase whereas the wide-angle scattering in the  $L_\alpha$  phase consists only of broad diffuse scattering. However, the analysis in this paper suggests that diffuse scattering is at least as great as peak scattering, implying that there is still considerable disorder in the gel phase even though the chains are rotamerically ordered.

Our analysis indicates that the disorder is relatively greater in the head group region than in the chain region. This is consistent with the picture that the head groups remain disordered. We might mention that we first attempted to accommodate the small satellite peaks at  $18.9^\circ$  and  $20.1^\circ$  by considering supercells corresponding to head group ordering, but that no satisfactory supercell was found.

Our analysis also suggests that there is disorder in the chain region. The usual interpretation of chain disorder in the gel phase is that there is free rotation of each chain around its long axis. There is recent evidence that this rotational disorder is not complete [30] and the ensuing short range correlations would contribute to the diffuse scattering. Of course, translational fluctuations must also be considered.

The study of disorder in lipid bilayers is relatively new and this paper only begins to come to quantitative grips with it. We considered a very primitive model for head group disorder in Sec. VIII that concentrates upon the positional disorder inherent in the fact that each molecule consists of two chains and one head. Not surprisingly, this primitive model does not do very well at reproducing the diffuse scattering indicated in Fig. 1, although it does provide a mechanism for producing diffuse scattering at angles considerably smaller than the region around the peaks. One might expect chain disorder to dominate diffuse scattering in the wide-angle peak region and the head groups to dominate the scattering at angles between the wide-angle peak region and the low-angle lamellar peaks.

In contrast to the study of disorder, we now believe that the study of the order in gel phase DPPC is rather complete. Our recent work [16] on fully hydrated oriented DPPC bilayers obtained the tilt angle  $\theta_t$  to be  $32^\circ$  at  $19^\circ\text{C}$  and verified directly that the tilt is towards nearest neighbors. The present paper obtains essentially the same results for fully hydrated unoriented samples; the slightly smaller value of  $\theta_t$  obtained here is consistent with the data having been taken at  $24^\circ\text{C}$  and with  $\theta_t$  decreasing with increasing temperature [16]. The present paper also obtains a number of additional results that could not be obtained from the oriented samples. These results are listed in Table I and include the models in Figs. 2 and 6. The fitted result for the length  $L$  of the hydrocarbon chains is in good agreement with that demanded by stereochemistry and the vertical extent of

the head-group positions agree with low-angle analyses [18]. One feature that we discovered is that the hydrocarbon tails in the two monolayers are slightly offset. This is not a surprising feature since there are no covalent bonds between the lipids in adjacent monolayers, but it has not been included previously in diffraction analyses. Some consequences of this feature for scattering are shown in Fig. 5. Additional results for bilayer structure are also derived and shown in Table II. It should be emphasized, however, that our data require registry between both monolayers of the bilayer, so that the effective chain length for scattering is basically  $2L$ , in agreement with our less accurate results from oriented samples [16].

The key to being able to obtain so much information from unoriented samples was obtaining quantitative data for the satellites and incorporating these data in the analysis. These satellites were originally reported by Mitsui and co-workers [9]. Although the original interpretation was incorrect, a brief correction was later noted [23], but no previous paper has included these satellites in a global analysis of the peak scattering.

Our result that the chains are tilted toward nearest neighbors disagrees with the conclusions of a recent study in which the DPPC bilayers were oriented on a glass beaker [6]. Their geometry precluded tilting the sample, an option that allows all wide-angle peaks to be observed with little differential absorption as we have recently shown [16]. The reported presence [6] of only one unique reflection that is off the equator is similar to the result of an earlier study at low hydration [13], where it was shown that this pattern corresponds to a uniform distribution of tilt directions. Our data, however, clearly have two unique reflections with a sharp (20) peak on

the equator for both unoriented samples and oriented samples on a glass substrate [16]. It may also be useful to compare to results on free-standing films of dimyristylphosphatidylcholine (DMPC) [12], where it was carefully shown that the direction of tilt could be towards neighbors (as in the present paper), between neighbors (two unique off-equatorial reflections), or even between the preceding two cases (three unique off-equatorial reflections), depending upon hydration. Although full hydration conditions were not achieved, extrapolation using the reported phase diagram [12] suggests that the fully hydrated gel phase would have the chains tilted between neighbors rather than towards neighbors as we find for DPPC. Our unpublished data for DMPC also indicate that the tilt is towards neighbors because there is again one narrow and one broad wide-angle peak. An explanation for this variety of results is that differences in free energies for different directions of chain tilt may be small so that the observed chain tilt direction may be highly sensitive to sample preparation including the influence of substrates. We suggest that the unoriented samples studied in this paper are least susceptible to these influences, so that the results reported here are more appropriate for model membranes.

#### ACKNOWLEDGMENTS

We thank Tom Irving and Ernie Fontes for performing exploratory and confirmatory studies with one of us (C.R.W.) at CHESS and to Joe Schindler for exploratory studies at CMU. This research was supported by Grant No. GM-44976 from the US National Institutes of Health.

- 
- [1] A. Blaurock and T. McIntosh, *Biochemistry* **25**, 299 (1986).
- [2] G. Buldt, H. U. Gally, J. Seelig, and G. Zaccai, *J. Mol. Biol.* **134**, 673 (1979).
- [3] S. Hui, *Chem. Phys. Lipids* **16**, 9 (1976).
- [4] M. Hentschel and F. Rustichelli, *Phys. Rev. Lett.* **66**, 903 (1991).
- [5] M. J. Janiak, D. M. Small, and G. G. Shipley, *Biochemistry* **15**, 4575 (1976).
- [6] J. Katsaras, D. S.-C. Yang, and R. M. Epand, *Biophys. J.* **63**, 1170 (1992).
- [7] Y. K. Levine, Ph. D. thesis, University of London, 1970.
- [8] T. J. McIntosh, *Biophys. J.* **29**, 237 (1980).
- [9] T. Mitsui, *Adv. Biophys.* **10**, 97 (1978).
- [10] J. F. Nagle, *Ann. Rev. Phys. Chem.* **31**, 157 (1980).
- [11] J. F. Nagle and D. A. Wilkinson, *Biophys. J.* **23**, 159 (1978).
- [12] G. S. Smith, E. B. Sirota, C. R. Safinya, and N. A. Clark, *Phys. Rev. Lett.* **60**, 813 (1988).
- [13] J. B. Stamatoff, W. F. Graddick, L. Powers, and D. E. Moncton, *Biophys. J.* **25**, 253 (1979).
- [14] A. Tardieu, V. Luzzati, and F. C. Reman, *J. Mol. Biol.* **75**, 711 (1973).
- [15] J. Torbet and M. H. F. Wilkins, *J. Theor. Biol.* **62**, 447 (1976).
- [16] S. Tristram-Nagle, R. Zhang, R. M. Suter, C. R. Worthington, W.-J. Sun, and J. F. Nagle, *Biophys. J.* **64**, 1097 (1993).
- [17] D. C. Wack and W. W. Webb, *Phys. Rev. A* **40**, 1627 (1989).
- [18] M. C. Wiener, R. M. Suter, and J. F. Nagle, *Biophys. J.* **55**, 315 (1989).
- [19] M. C. Wiener and S. H. White, *Biophys. J.* **61**, 434 (1992).
- [20] C. R. Worthington and R. S. Khare, *Biophys. J.* **23**, 407 (1978).
- [21] J. B. Stamatoff, H. J. Feuer, B. Guggenheim, G. Tellez, and T. Yamane, *Biophys. J.* **38**, 217 (1982).
- [22] M. Hentschel and R. Hosemann, *Mol. Cryst. Liq. Cryst.* **94**, 291 (1983).
- [23] Y. Inoko, T. Mitsui, K. Ohki, T. Sekiya, and Y. Nozawa, *Phys. Status Solidi* **61**, 115 (1980).
- [24] N. D. Mermin, *Phys. Rev.* **176**, 250 (1972).
- [25] P. Dutta and S. K. Sinha, *Phys. Rev. Lett.* **47**, 50 (1981).
- [26] W. H. Zachariasen, *Theory of X-ray Diffraction in Crystals* (Wiley, New York, 1945).
- [27] C. W. Bunn, *Trans. Faraday Society* **35**, 482 (1939).
- [28] J. F. Nagle and M. C. Wiener, *Biochim. Biophys. Acta* **942**, 1 (1988).
- [29] M. C. Wiener and S. H. White, *Biophys. J.* **61**, 428.
- [30] J. F. Nagle, *Biophys. J.* **64**, 1110 (1993).

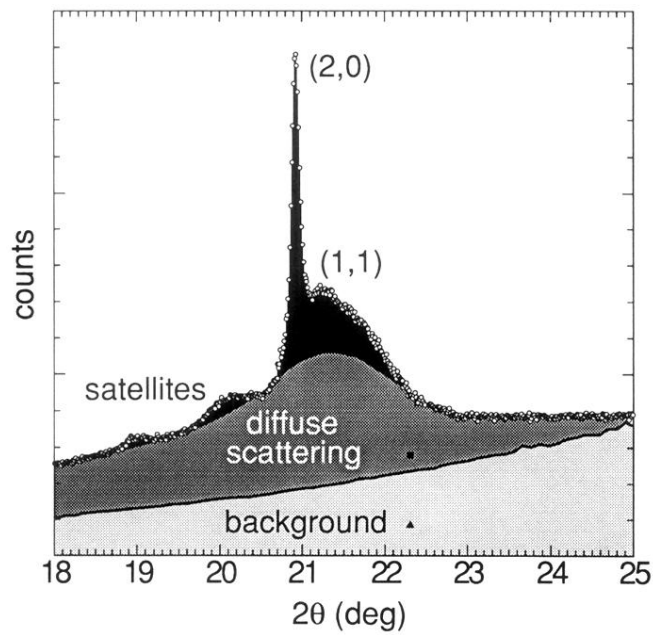


FIG. 1. Wide-angle scattering intensity versus scattering angle  $2\theta$  (open circles) taken with graphite monochromator and PSD 572 mm from the sample. Slits were configured to yield resolution  $0.068^\circ$  HWHM, which is the width of the unresolved (20) peak. The area in black is interpreted as the peak scattering. The temperature was  $24^\circ\text{C}$ . At  $2\theta = 22.3^\circ$  the solid square shows the scattering from a capillary filled with water and the solid triangle shows the scattering from a capillary in air.